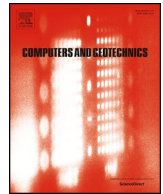




ELSEVIER

Contents lists available at ScienceDirect

Computers and Geotechnics

journal homepage: www.elsevier.com/locate/compgeo

Research Paper

Effects of barrier deformability on load reduction and energy dissipation of granular flow impact

C.W.W. Ng^a, C. Wang^a, C.E. Choi^{b,*}, W.A.R.K. De Silva^a, S. Poudyal^a^a Department of Civil and Environmental Engineering, The Hong Kong University of Science and Technology, Hong Kong Special Administrative Region^b Department of Civil Engineering, The University of Hong Kong, Hong Kong Special Administrative Region

ARTICLE INFO

Keywords:

Granular flow
Impact
Deformable barrier
Flexural rigidity
Material point method
Energy dissipation

ABSTRACT

Granular flows, such as debris flows, are commonly arrested by using deformable barriers, but their designs rely heavily on empiricism. The fundamental impact mechanisms between a granular flow and a deformable barrier have yet to be elucidated. Thus, estimating the impact load on deformable barriers remains a key scientific and engineering challenge. In this paper, the material point method (MPM), with the Drucker-Prager yield criterion associated with a linear elastic model is calibrated against physical model tests. The effects of barrier deformability on the impact force induced by a granular flow are examined. For simplicity, a vertical and deformable cantilever barrier with different flexural rigidity is simulated. The dissipation of energy of a frictional granular assembly subjected to shear is considered in the simulation. A threshold $3EI/H^3_{\text{norm}} = 6.3 \times 10^{-5}$ (normalized by the stiffness of a typical 1-m thick reinforced concrete cantilever barrier) is identified in this study to demarcate between rigid and deformable barriers. A maximum deformation of only 3% of the total barrier height and corresponding reduced relative velocity are enough to attenuate the peak impact load by 40% compared to a rigid barrier. Around 85% of the dissipated energy occurs during the pile-up process, the interaction between the incoming flow and deposited material along the slip interface is effective in dissipating flow kinetic energy.

1. Introduction

Rapid granular flows, such as debris flows and rock avalanches, are among the most destructive geo-hazards that occur in mountainous regions. Various protective structures, including check dams, reinforced concrete barriers and flexible steel net barriers, are commonly installed along predicted flow paths to arrest these geo-hazards [1,2]. Barriers can be characterized as either rigid or deformable [3]. The dynamic interaction between granular flows and an obstacle is a complex scientific problem because of the rheological behavior of granular material subjected to shear. This means that an appropriate constitutive model is required to capture its complex shear response. Without a clear understanding of the fundamental mechanisms of interaction between granular flows and barriers, engineering design cannot progress from empirical-based to semi-empirical approaches.

The most commonly used approach to estimate the impact load is the force approach [4], which utilizes the hydrodynamic equation to predict impact force F induced by the flow:

$$F = \alpha \rho v_f^2 \cos \theta h w \quad (1)$$

where α is an impact coefficient; ρ is the bulk density of the flow with a suggested minimum value 2200 kg/m^3 [4,5]; v_f is the velocity of the

flow before impact; h is the flow depth before impact; w is the channel width and θ is the impact angle between the flow and barrier surface normal. If α is unity, then the impact scenario is considered inelastic. Conversely, if α is two, then the impact scenario is considered elastic, constituting a theoretical upper bound scenario. The contact area in Eqn. 1 is idealized and assumed to remain unchanged during the impact process. However, in reality granular materials induce both static and dynamic loading with a load distribution and impact area governed by the prevailing impact mechanism. To ensure a robust barrier design, international guidelines often prescribe even higher α values to account for the idiosyncrasies of natural materials and settings involved during an impact, and the complex impact mechanisms that Eqn. 1 cannot capture. For example, Kwan [4] recommends an α of 2.5 for the design of rigid reinforced concrete barriers and an α of 2.0 for the design of flexible barriers for resisting debris flows. Aside from the force approach, the energy approach proposed by Kwan is also used for design. The energy approach assumes that the flow kinetic energy is entirely absorbed by the barrier. However, Ng *et al.* [5] carried out centrifuge tests on a deformable barrier and reported that only up to 15% of the flow kinetic energy is absorbed by barrier deformation, the rest of the energy was predominantly dissipated via internal grain shearing.

Various experimental and numerical studies have been conducted

* Corresponding author.

over the past decade to study the interaction between granular flow and barriers based on force [6–8] and energy approaches [9]. However, existing studies mainly focused on rigid structures whereas deformable structures are rarely investigated [10]. Given the importance of internal energy dissipation of the granular assembly during the impact process as the barrier deforms, a proper numerical tool with an appropriate constitutive behavior that captures the shear response of the granular material is needed.

The most commonly adopted approach for modelling granular flows is by assuming an equivalent fluid and using a depth-averaged solution [11–13]. However, a depth-averaged solution has limitations in modelling the vertical momentum transfer during an impact scenario. Furthermore, the shearing behavior of a granular material is not captured. Another emerging numerical tool for studying the impact dynamics of granular flows on barriers is the discrete element method (DEM) [14]. Iverson [15] described two approaches to describe the dynamics of granular flows. Granular flows can be analysed at a macroscopic level, which considers the entire complex mixture of grains as a continuum, and at a mesoscopic level, which considers the interactions among grains, and between grains and the pore fluid. Although the DEM can explicitly capture mesoscopic interactions, it requires a multitude of input parameters that can be difficult to obtain and calibrate. More importantly, balancing between accuracy and computational costs of DEM remains its fundamental limitation. For the fine particles simulated in this study, the impulsive loading given by the coarse particles does not appear and the continuum based method can be a feasible approach to be adopted. Alternatively, the material point method (MPM) proposed by Sulsky [17] combines the advantages of both depth-averaged methods and DEM, especially the ability to capture bifurcation [18,19], which is an important feature to model when studying flow-structure interaction. Furthermore, the MPM is computationally effective and enables the material points to adopt non-local constitutive laws for modelling flows with different particle sizes [20]. Ceccato *et al.* [16] reported that a simple elastoplastic model can capture the shear behavior of dense flows impacting against rigid barriers. The capabilities of the MPM in modelling other soil-structure interaction problems [17–19] have highlighted the convenience of the MPM for problems where contact interfaces need to be traced, such as an impact problem. Evidently, the MPM is a suitable tool for modeling the impact dynamics of granular flows against deformable barriers.

In this study, a Drucker-Prager yield criterion associated with a linear elastic model is implemented into an open source MPM code [20]. This code framework is developed by Prof. John A. Nairn. The calculation framework is object-oriented c++ code engine, which is highly versatile and easy to modify. Generalized interpolation law is adopted in this study to avoid the crossing grid noise. Coulomb friction law is adopted to handle the interface friction between two objects [20]. This code has been widely applied in simulating engineering problems like Orthogonal Cutting [20,21], 3D crack propagation [22] and installation of jacked piles in sand [23]. Recently, Liang and Zhao [24] has coupled this code to YADE and proved the feasibility of this code in the geotechnical applications. The newly implemented code is calibrated using physical experimental data [25]. The calibrated MPM model is then used to carry out a parametric study to discern the effects of barrier flexural rigidity on the impact dynamics against a deformable barrier. For simplicity, a vertical deformable cantilever barrier with varying flexural rigidities are simulated.

2. Material point method (MPM)

The MPM is used in this study to model the dynamics of dry granular flow impacting barriers. The MPM discretizes objects into material points. The motion of these points are governed by the momentum equation:

$$\rho \frac{D\mathbf{v}_p}{Dt} = \nabla \cdot \boldsymbol{\sigma} + \rho \mathbf{b} \quad (2)$$

where ρ is the density, \mathbf{v}_p is the particle velocity, $\boldsymbol{\sigma}$ is the Cauchy stress tensor, \mathbf{b} is the specific body force and ∇ is the gradient tensor. Each material point does not represent an individual grain but a continuum that behaves according to a pre-defined constitutive model (to be discussed). Each material point carries mass, velocity, stress and strain. At each time step, the information carried by a material point is mapped onto the nodes of a background mesh and this information is used to deduce the velocity field. Afterwards, the velocity is extrapolated back to each material point to update its velocity and position [26].

2.1. Drucker-Prager yield criterion associated with a linear elastic model

The constitutive behavior implemented for the granular material in this study is the Drucker-Prager (DP) yield criteria with a linear elastic model. The yield surface of the DP model [27] can be expressed as follows:

$$f = s - \sqrt{2} q_\phi \sigma_m - \sqrt{2} k_\phi \quad (3)$$

where $s = \sqrt{2J_2}$; $\sigma_m = \frac{1}{3}\text{tr}(\boldsymbol{\sigma})$ is the spherical pressure and $\boldsymbol{\sigma}$ is the Cauchy stress tensor. $J_2 = \frac{1}{2}\mathbf{s}:\mathbf{s}$ represents the second invariant of deviatoric stress tensor $\mathbf{s} = \boldsymbol{\sigma} - \sigma_m \mathbf{I}$, and \mathbf{I} is the identity tensor; q_ϕ is the coefficient of friction, which controls the influence of spherical stress on the size of the yield surface, and k_ϕ is the yield stress under pure shear. Correspondingly, q_ϕ and k_ϕ can be calculated as follows [28]:

$$q_\phi = \frac{2\sin(\phi)}{\sqrt{3}(3 - \sin\phi)} \quad k_\phi = \frac{2\sqrt{3}\cos\phi}{(3 - \sin\phi)} \quad (4)$$

For large deformation problems, a stress rate invariant to rigid-body rotation must be employed [28]. Correspondingly, a Jaumann stress rate $\dot{\boldsymbol{\sigma}}_{ij}^{\nabla}$ is adopted as follows:

$$\dot{\boldsymbol{\sigma}}_{ij}^{\nabla} = \dot{\sigma}_{ij} - \sigma_{ik}\omega_{jk} - \sigma_{jk}\omega_{ik} \quad (5)$$

where $\dot{\sigma}_{ij}$ is the Cauchy stress rate tensor and ω is the angular velocity.

Coulomb's Law [29,30] was adopted to model the interaction between the granular flow and the channel. An interface friction coefficient 0.4 was adopted based on measurements reported by Ng *et al.* [25]. The Young's modulus for sand was set to be 1 MPa based on that recommended by Bui *et al.* [31]. A Poisson's ratio 0.3 and internal friction angle 31° were adopted for the granular material. In this study, a relatively small value of PIC fraction ($\alpha_{\text{PIC}} = 5 \times 10^{-4}$) is adopted to provide the necessary computational stability while satisfying energy conservation [24]. Details of the approach used to update the velocity can be found in Appendix A. Additionally, four material points were used for each element [32]. A summary of relevant input parameters is given in Table 1.

2.2. Numerical model setup and simulation plan

Fig. 1 shows the numerical model setup used in this calibration. The setup is geometrically identical to that reported in the physical experiments by Ng *et al.* [25]. The model channel is inclined at $\theta = 40^\circ$. The channel has a length, width and depth of 1.2 m, 0.2 m and 0.6 m, respectively. A container at the upstream end of the channel is used to

Table 1
Input parameters.

Young's modulus E (MPa)	1
Internal friction angle ϕ ($^\circ$)	31
Poisson's ratio ν	0.3
Interface friction coefficient μ	0.4
Damping coefficient α_{PIC}	5×10^{-4}
Gravitational acceleration g (m/s 2)	9.81

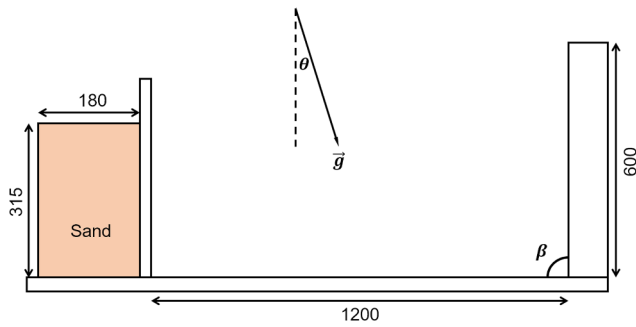


Fig. 1. Numerical model setup (all dimensions are in mm).

store the granular material, which is retained behind a gate that is 0.5 m in height. A 0.6 m tall barrier is installed perpendicularly to the flume at a distance of 1.2 m from the gate. Both the flume and barrier are modeled as rigid walls as the MPM model is calibrated.

For each analysis, material points were generated in the storage container before applying gravity to the computational domain to allow material points to reach static equilibrium. The channel was then inclined to 40° before the granular mass was released down the flume. The interaction between the barrier and flow was modelled with two velocity fields by using the multi-material mode [20], which enables contacts to be detected so that the impact load can be computed.

After calibrating the MPM model against physical experiments, an additional simulation was carried out at a flume inclination of 60° to simulate a more inertial flow. In order to keep the barrier vertical, the intersection angle between flume and barrier $\beta = 30^\circ$. At such a steep inclination, a sharp peak load was generated followed by load reduction to a static load. The cantilever barrier 0.6 m in height, 0.2 m in width and 0.1 m in thickness to simulate reinforced concrete barrier. The second moment of area of the cantilever concrete barrier is $1.7 \times 10^{-5} \text{ m}^4$.

The Young's modulus of the rigid barrier is 25 GPa to model reinforced concrete. The flexural rigidity $4.2 \times 10^8 \text{ N}\cdot\text{m}^2$ is calculated by assuming a typical 1 m-thick reinforced concrete barrier, which is used to normalize the flexural rigidity of other barriers in this study. Other barrier flexural rigidities are investigated by changing the Young's modulus. The stiffest barrier used in this study is equivalent to a 5 mm-thick steel plate and the softest barrier used in this study is equivalent to a 5 mm-thick plastic plate. A summary of the barrier flexural rigidity adopted is given in Table 2.

3. Calibration and evaluation of MPM model

The MPM model implemented in this study is evaluated with experimental data reported by Ng *et al.* [25]. The simulated impact kinematics and dynamics were compared with that observed and measured, respectively. In the physical experiment, a total mass of 30 kg of Leighton Buzzard Fraction C sand, with a fairly uniform particle size of 0.6 mm was used to model the granular material. The impact load was

Table 2
Summary of flexural rigidity of barriers with typical equivalent material.

$E_b I_b (\text{N}\cdot\text{m}^2)$	$3EI/H^3_{\text{norm}}$	Equivalent material for barrier
8.33	2.5×10^{-6}	Plastic barrier with $E = 4 \text{ GPa}$ (5 mm-thick)
3.33×10^1	1×10^{-5}	Fibre glass barrier with $E = 16 \text{ GPa}$ (5 mm-thick)
1.67×10^2	5×10^{-5}	Aluminum alloy barrier with $E = 80 \text{ GPa}$ (5 mm-thick)
3.33×10^2	1×10^{-4}	Steel alloy barrier with $E = 160 \text{ GPa}$ (5 mm-thick)
4.17×10^8	1	Concrete barrier with $E = 25 \text{ GPa}$ (1 m-thick)

$3EI/H^3_{\text{norm}}$ is the cantilever barrier stiffness normalized by the stiffness of cantilever concrete barrier with typical thickness of 1 m and height of 3 m.

measured from a load cell sandwiched between the barrier and a reaction frame mounted in the flume.

Fig. 2 shows a comparison between the observed and computed impact kinematics. The velocity fields from the physical experiments were analyzed using particle image velocimetry PIV [33]. The monitoring area is just 500 mm upstream from the barrier for comparing kinematics. The PIV is compared with computed velocity contours from the MPM simulations. The time is taken as $t = 0 \text{ s}$ when the flow just approaches the barrier. The calculated maximum frontal velocity of the granular flow is 2.2 m/s before impact, corresponding to a Froude number $Fr = 3.5$. The Fr matches well with that observed in the physical tests. At $t = 0.6 \text{ s}$, the maximum velocity reduced by more than 40% to 1.4 m/s. After impact, the granular material accumulates at the base of the barrier, forming a dead zone [5,34]. Subsequent granular material impacts the ramp-like dead zone and piles up on top to increase the total static load acting on the barrier. Meanwhile, the flow kinetic energy is dissipated as shearing occurs between the flowing and deposited material. At $t = 0.9 \text{ s}$, the maximum velocity is 0.8 m/s and the flow starts to reach static equilibrium. The maximum velocity deduced by using PIV shows only a small difference of 17% compared to that computed. The profile of the simulated final deposition differs slightly from that observed. Differences are mainly caused by the constitutive model, which neglects the softening behavior of the granular assembly and assumes a constant Young's modulus. Notwithstanding, the general impact mechanisms, such as the formation of a dead zone and subsequent pileup, appear to be well-captured by the MPM model.

To examine changes in energy during impact, the total energy from each MPM simulation is decomposed into potential, kinetic and strain energies. Kinetic energy E_k is calculated as follows:

$$E_k = \frac{1}{2} \sum_{i=1}^N m_i v_i^2 \quad (6)$$

where N is the total number of the material points, m_i is the mass of each material point, and v_i is the velocity of each material point. During the flow and impact process, aside from the conversion from potential to kinetic energy, energy is also dissipated via internal and basal shearing in the granular assembly. The strain energy E_s to describe the dissipative work done by plastic shearing is calculated as follows:

$$E_s = \int \epsilon : \sigma dv \quad (7)$$

where σ is the total stress tensor stored in each material point and ϵ is the total strain evaluated at each material point. In addition to the internal energy dissipated from the continuum body, basal friction also does work to the granular assembly. This work is the sum of the product of the frictional force and the distance travelled by all near boundary material points.

Fig. 3 shows the changes in energy within the granular assembly. The authors normalize each energy by the initial potential energy E_0 of the granular material before initiation and the datum is taken at the base of the barrier. As the granular assembly flows down the incline, the potential energy decreases as it is partly converted into kinetic energy. About 90% of the initial potential energy is dissipated via internal and basal friction. Since energy dissipation cannot be directly measured in the physical experiments, a comparison of changes in energy between the numerical simulation and physical experiments can only be carried out in terms of kinetic energy. According to Thielicke [35], the full velocity field can be gained by using PIV analysis. After getting the velocity data of the flow, the average velocity can be calculated to obtain the kinetic energy at each time step (Fig. 2). Fig. 3 shows the measured kinetic energy from the experimental data at three different snapshots shown in Fig. 2. The first snapshot focuses on the frontal part of flow, which has a higher velocity compared to the rest of the flow body. As a result, the estimated kinetic energy at time $t = 0.2 \text{ s}$ is 40% larger than that calculated. For the data point estimated at $t = 0.8 \text{ s}$ and 1.1 s , the majority of flow body is included in the frame and the

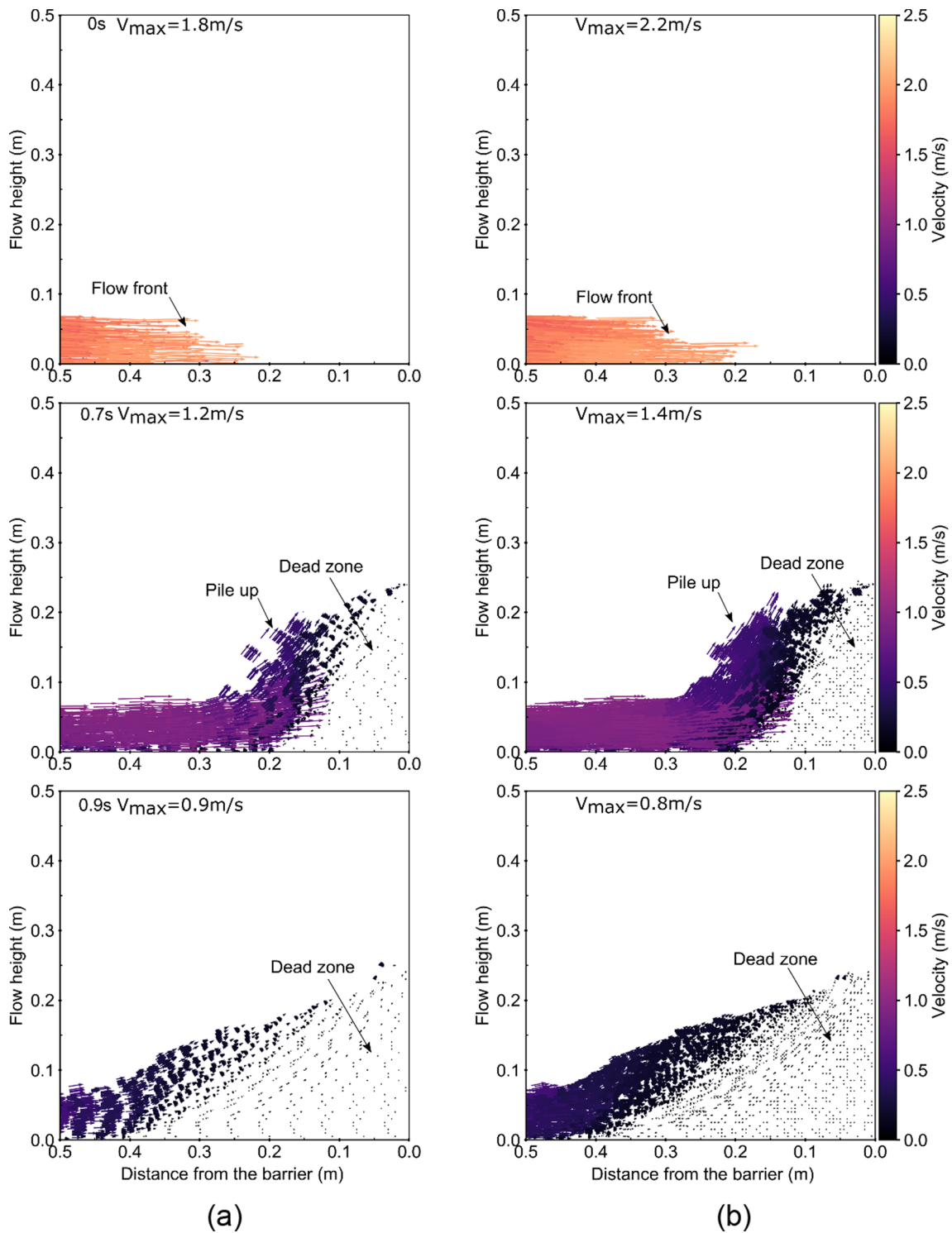


Fig. 2. Comparison of impact kinematics against rigid barrier (all dimensions are in mm): (a) PIV of high-speed camera images from experiments (Ng et al. [25]); (b) computed velocity contours from MPM simulation.

estimated kinetic energy is only 10% less or more than that measured. Aside from comparing the impact kinematics, the impact dynamics also need to be evaluated for the MPM model. Fig. 4 shows a comparison between the force–time histories measured from the physical experiments [25] and computed by the MPM model. The impact force in the MPM model is calculated as follows:

$$F(t) = \sum_{i=1}^M P_i(t)A_i(t) \quad (8)$$

where $P_i(t)$ and $A_i(t)$ are the impact pressure and area between the flow and barrier, respectively, and M is the number of material points in contact with the barrier. The interface between the granular flow and the deformed barrier can be detected during deformation [20]. The pressure is extracted from the area along the interface with the thickness of two material points. Both inclinations of 23° and 40° in the experiments [25] are evaluated in this study. For an inclination of 23° (Fig. 4a), the impact force increases progressively after impact until it reaches a static state after 0.5 s. The maximum load is the static force,

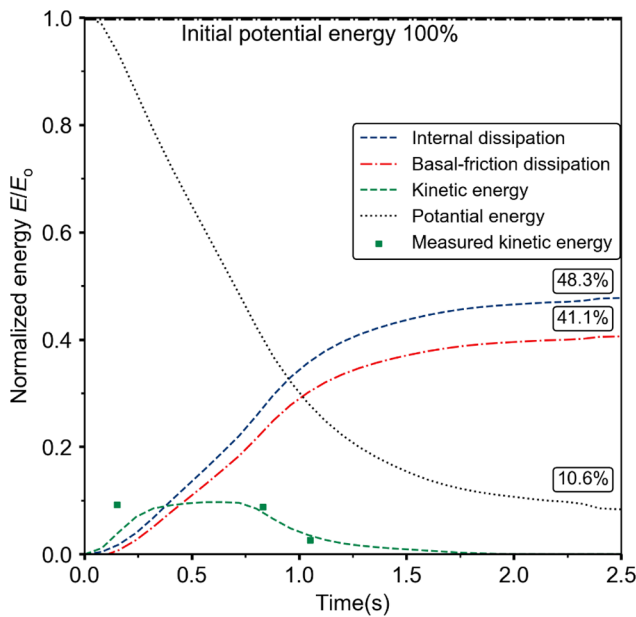


Fig. 3. Energy evolution inside granular flow of barrier inclination angle of 40°.

which is 55 N. The computed static force is only 10% larger than that measured. The inclination of 23° is close to the basal interface frictional angle, which is 22°, thus the basal interface friction slows down the flow, resulting in subdued impact dynamics. In Fig. 4(b), the computed impact force resulting from an inclination of 40° shows a similar trend to that observed for an inclination of 23° whereby the load increases progressively before reaching a static state. The impact force is normalized by the theoretical static force of 99 N, following the approach reported by Moriguchi et al. [6]. The computed impact force also gradually increases to a static loading of 87 N after 1.8 s, which is close to the maximum value of 79 N.

The effects of considering energy dissipation via internal shearing can be shown by comparing the difference in impact loads measured and that calculated using Eqn. 1, which does not consider internal shearing in the granular assembly. Correspondingly, Eqn. 1 over-predicts the impact force by up to 30% compared to that measured. Furthermore, a comparison is also made with an analytical model proposed by Albaba et al. [8], which is dependent on the input flow velocity. Their model considers energy dissipation before impact by changing the incoming velocity. The general trend between the computed and calculated results are similar. However, the proposed analytical model assumes a zero-length granular jump and does not explicitly consider momentum transfer between the incoming flow and the dead zone. As a result, this analytical model tends to over-predict the impact load.

The MPM model has been validated by the kinematics and dynamics of the granular flow impacting on rigid barrier from physical experiments. The comparisons give confidence that the MPM model in this study is appropriate for conducting a parametric study to examine the effects of barrier flexural rigidity on the impact dynamics of granular flow.

4. Interpretation of computed results

4.1. Effects of flexural rigidity on barrier deformation and impact dynamics

Fig. 5(a) shows the impact pressure time histories extracted from four typical barriers as shown in Table 2. For each barrier flexural

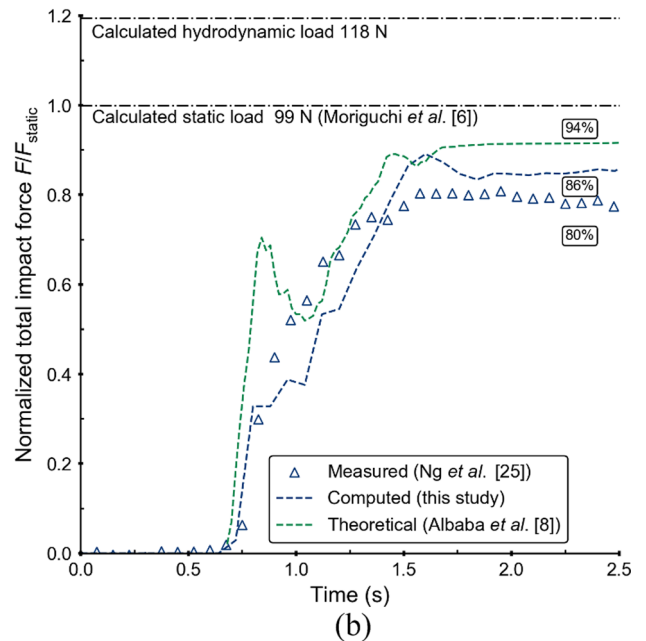
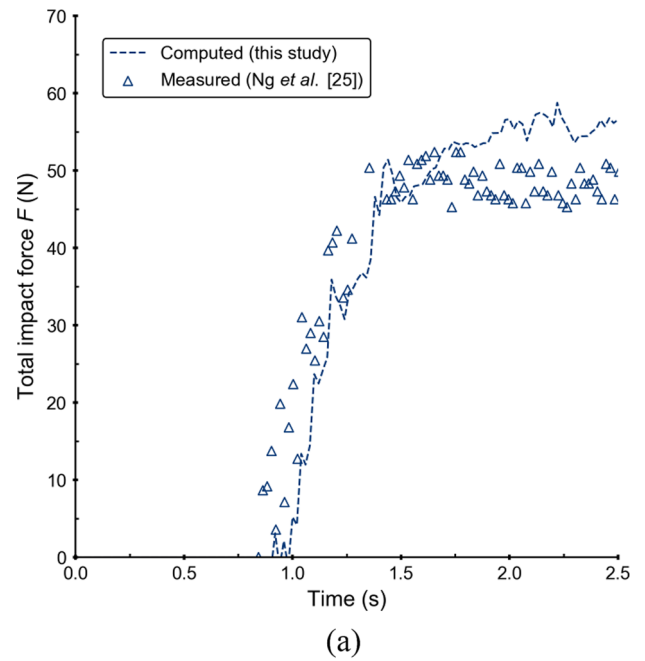


Fig. 4. Comparison of total impact forces on rigid barrier with different inclination angles (a) 23° and (b) 40°.

rigidity, the pressure time history shows a dynamic impact peak pressure, which then decreases to the static lateral earth pressure as the granular material reaches a static state. A peak pressure is clearly observed for the steel barriers and becomes less obvious with a decreasing barrier stiffness. In order to choose a consistent peak pressure time, the pressure time history within a smaller time range (0.62 s–0.82 s) is shown. As the simulation data is archived every 0.02 s, Fig. 5(b) shows the data points plotted at each archived time step. Although the peak pressure time can be slightly different if a smaller archiving time is chosen, Fig. 5(b) can show the clear peak for different barrier flexural rigidities and the peak pressure time is shown to be 0.66 s.

Fig. 6 shows the effects of barrier flexural rigidity on the impact

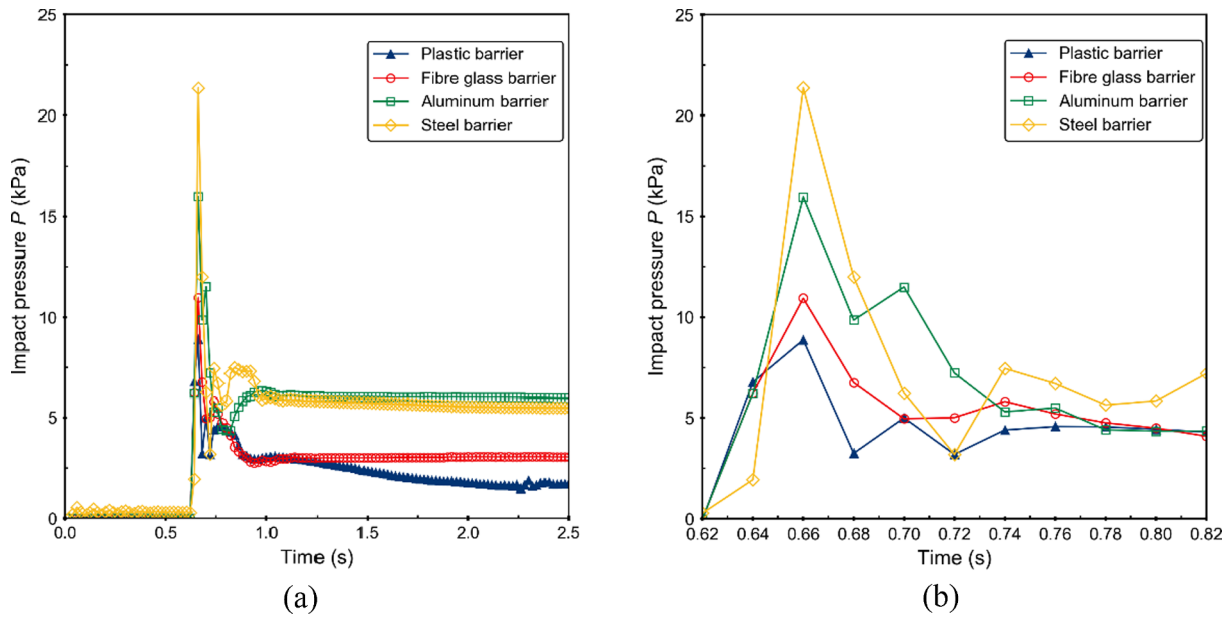


Fig. 5. Impact pressure time history and the peak value.

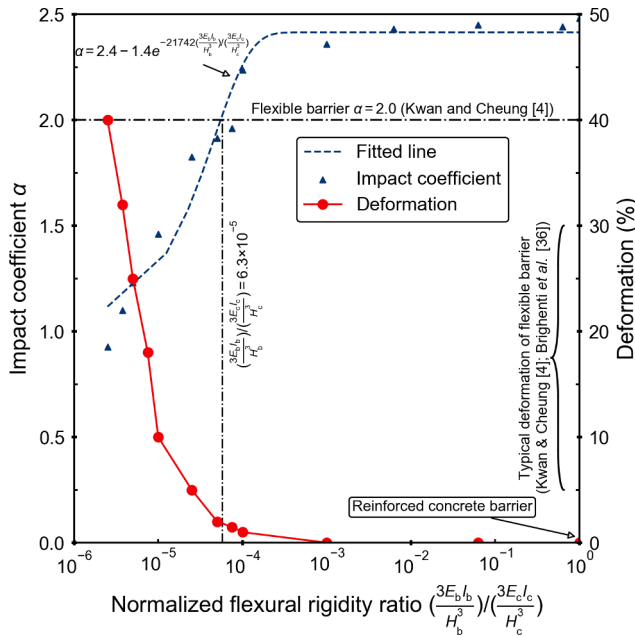


Fig. 6. Effects of barrier flexural rigidity on the impact coefficient α .

load by using the impact coefficient α . Additionally, the final barrier deformation is also shown, and the range of deformation is from 0% (reinforced concrete barrier) to 40% (deformable barriers) [36]. Twelve different normalized flexural rigidities ranging from 1×10^{-6} to 1 were simulated. A comparison of simulated results shows that the impact coefficient α increases with normalized flexural rigidity ranging from 1×10^{-6} to 5×10^{-3} . As expected, the impact coefficient α increases with normalized flexural rigidity ranging from 1×10^{-6} to 5×10^{-3} . Conversely, the deformation decreases with the increase in normalized flexural rigidity.

Existing design guidelines [4] provide recommended impact coefficients α to differentiate between rigid ($\alpha = 2.5$) and flexible barriers ($\alpha = 2.0$). However, it may not be easy to assess whether a barrier

should be considered as rigid or flexible. Even a flexible barrier with very stiff brake elements or high pretension loads in the cables may behave as a rigid barrier. Furthermore, a wide range of deformable barriers with different loading behaviors exist around the world. The MPM simulation of the plastic-like barrier with a very small flexural rigidity ($3EI/H^3_{norm} = 2.5 \times 10^{-6}$) may be treated as flexible barrier in design since the back-calculated impact coefficient α is 2.3, which exceeds the recommended value for flexible barriers according to Kwan [4]. The intersection point between the back-calculated impact coefficients α and the recommended design value for a flexible barrier corresponds to a normalized flexural rigidity 6.3×10^{-5} . Evidently, the recommended values in design are not necessarily conservative for the design of a flexible barrier with a small amount of deformation to maintain the structure integrity [37]. There is a noticeable change in dynamic response when the flexural rigidity is larger than that of a steel-like barrier ($3EI/H^3_{norm} = 1.0 \times 10^{-4}$). Eventually both the calculated impact coefficients α and barrier deformation start to converge. At a normalized flexural rigidity 1.0×10^{-3} , the deformation of the barrier becomes negligible (less than 3% of barrier height; Fig. 9) and is reminiscent of a rigid barrier. This flexural rigidity can be regarded as a reference basis for engineers to demarcate between the impact behavior of a flexible and rigid barrier.

4.2. Reflection of pressure wave

Fig. 6 shows that the impact coefficient α increases with the flexural rigidity of the barrier. Eq. (1) is commonly used to estimate the impact force exerted on a barrier. However, this equation does not consider the transient nature of the impact process for a barrier with large deformation, which changes the impact angle as well.

The compressibility of the granular material also plays a significant role in regulating the impact load. Obviously, for a granular assembly that compresses, the impact scenario is inelastic [36]. To characterize the effects of flow compressibility, a pressure wave is used. During the very first few milliseconds after impact, a pressure wave propagates upstream with a celerity c . This pressure wave eventually decelerates and arrests the granular assembly. Therefore, the compressibility of the flow plays a major role in regulating the pressure wave and therefore

the impact force exerted on the barrier [38]. Based on the conservation of linear momentum, the peak pressure in the granular assembly can be calculated as follows:

$$P = \rho cv_0 \tag{9}$$

where c is dependent on the elastic modulus of both the material, ρ is its material density and v_0 is the incoming flow velocity. The celerity is defined as follows:

$$c = \sqrt{\frac{E}{\rho}} \tag{10}$$

To investigate the effects of barrier flexural rigidity on the propagation of a pressure wave in the granular assembly, flow stresses are computed at the peak load in each MPM simulation. The mean stress inside the granular flow is extracted from the grid just 0.2 m upstream from the barrier. The negative pressure has been observed in other two-phase continuum models when the granular assembly dilates ([39]). For dry sand, that there should not be any negative pressure. Studies ([40]) have been conducted to investigate the dissipation of the impact wave in granular material, which is highly related to the positive compression pressure and shearing process in the sand. Thus, a negative pressure was not observed in the simulations because the granular material is compressible and cannot sustain any tension due to the zero cohesion value

Fig. 7 compares the pressure wave propagation when a granular flow impacts the simulated plastic and steel barriers. The granular flow arrives at the barrier at $t = 0.66$ s. For the steel barrier, the induced pressure is 30% larger than that of the plastic barrier. At $t = 0.68$ s for both plastic and steel barriers, pileup is observed and the pressure wave has propagated about 0.2 m in the upstream direction of the barrier. The wave propagation inside the soil is highly dependent on the density of the material [40]. After impacting the barrier, stress is induced inside the flow. For a steel barrier with high stiffness, the large compression of the flow material rapidly increases the density of flow front and prevent the stress wave from dissipating. After propagation, the spike generated due to impact can still be observed at 0.08 m away from the barrier. While for the plastic barrier, the flow front is not compressed and so the debris is looser, thus it can easily dissipate the stress wave inside the granular flow and no spikes caused by stress wave are observed. The pressure wave for the steel barrier ($3EI/H^3_{norm} = 1.0 \times 10^{-4}$)

propagates upstream at a velocity of about 5 m/s, which is almost double the velocity computed for the plastic barrier ($3EI/H^3_{norm} = 2.5 \times 10^{-6}$) ($c_1 = 2.6$ m/s). The difference in pressure wave velocity implies that steel barriers are more effective at transferring stresses back upstream in the granular body. Therefore, momentum is more effectively reflected after impact. The pressure wave propagation helps to explain why the peak pressure differs depending on barrier flexural rigidity.

Although the celerity of steel barrier case can differ by up to two times than the plastic barrier, the estimated velocity of the pressure wave for steel barrier is only 5 m/s, which is much smaller than that in a fully elastic body (1600 m/s). The difference in velocity between plastic and steel barrier is due to the larger bulk compressibility of the granular assembly during impact against the steel plate barrier. Granular flow impacting a stiffer barrier experiences higher compression than that of a softer barrier, thus making the granular material denser and enabling higher celerity. The dampened celerity is indicative of the reduction in peak pressure caused by barrier deformation. However, celerity is not the sole reason for such a large reduction in impact load given the small magnitude of celerity inside the granular body.

4.3. Rate of barrier deformation

Equation 1 shows that the relative velocity between the flow and barrier also plays an important role in regulating the impact force. Therefore, the material points at the interface between the flow and barrier are tracked during each simulation. Fig. 8 shows the computed barrier velocities v normalized by the incoming flow velocity v_f at the peak impact time ($t = 0.68$ s). The vertical position h of each material point along the height of the barrier is normalized by the depth of the incoming flow h_f . When the normalized height is higher than 2.5, the incoming flow does not influence the barrier velocity and no obvious movement can be observed along the upper portion of the barrier. For the plastic barrier ($3EI/H^3_{norm} = 2.5 \times 10^{-6}$), which is the softest barrier simulated in this study, the maximum barrier velocity is 1.2 m/s, which corresponds to a relative velocity reduction of 40% compared to that of the flow before impact. The peak impact pressure also decreases up to around 40%, which results in the reduction of calculated

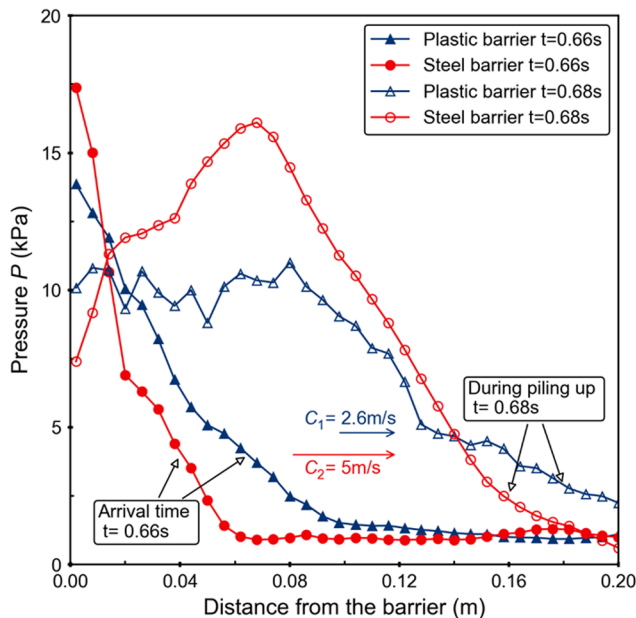


Fig. 7. Comparison of stress wave propagation for different barriers.

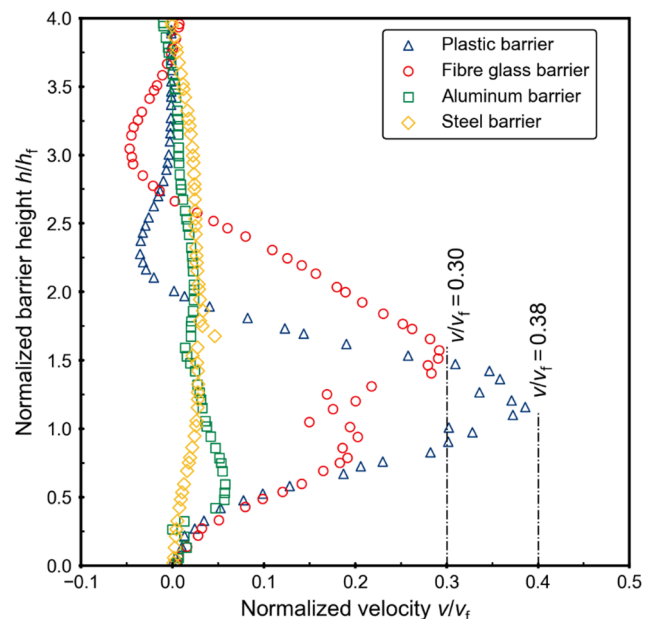


Fig. 8. Effects of barrier flexural rigidity on barrier velocity along the height of the barrier (barrier height normalized by incoming flow depth).

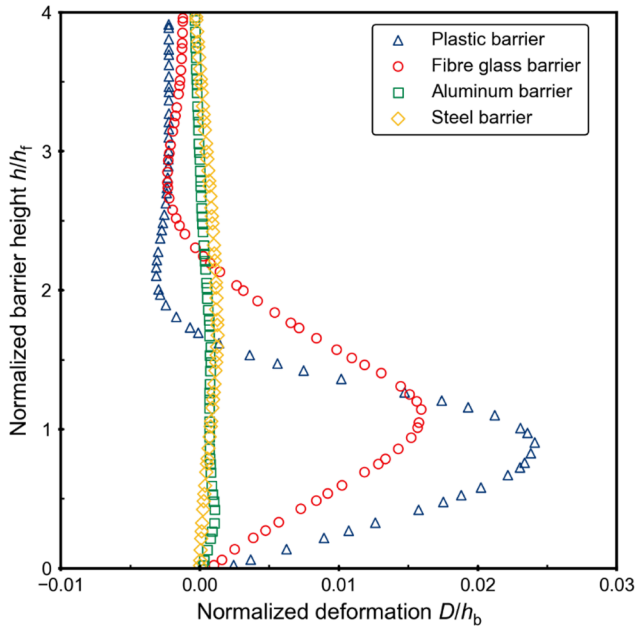


Fig. 9. The barrier deformation (normalized by barrier height) when the peak pressure occurs.

impact coefficient α shown in Fig. 6. A similar local velocity reduction is observed for the fiber glass barrier ($3EI/H^3_{\text{norm}} = 1 \times 10^{-5}$), which exhibits a velocity reduction of 30% compared to the initial velocity. In contrast with the softer barriers (plastic and fiber glass), not much velocity change occurs at the peak impact load for stiffer barriers (i.e. steel and reinforced concrete barriers). It is found that when the normalized flexural rigidity is larger than that of the steel barrier ($3EI/H^3_{\text{norm}} = 1 \times 10^{-4}$), localized velocity at the point of impact does not occur. This means that there is limited relative velocity between the flow and barrier, implying that deformable barriers should enable sufficient local relative velocity to attenuate the overall impact load.

At time $t = 0.68$ s, the barrier displacement due to the incoming flow is also tracked in each MPM simulation. Fig. 9 shows the deformation of the barrier as a percentage of the barrier height. The deformation is the ratio between barrier displacement D and initial barrier height h_b . The height of the tracked material points h is normalized by the incoming flow depth h_f . No deformation is observed at barrier heights less than twice that of the flow depth before impact. Deformation from impact mainly occurs at the bottom part of the barrier. It is generally accepted that the reason a flexible barrier can attenuate the impact pressure is because of large deformation. However, Fig. 9 shows that the barrier does not necessarily need to exhibit large deformation during the first few milliseconds of impact. For the plastic barrier, the maximum deformation is only around 3% of the total barrier height at the peak impact load. The stiffer barriers (i.e. steel and reinforced concrete barriers) barely deform at impact. Evidently, small deformations are enough to attenuate the peak pressure as long as local relative velocity between the flow and barrier occurs. This implies that initial slack of a on-site steel net barrier plays a significant role in regulating the peak pressure.

In addition to the deformation profile at the peak pressure for different barrier flexural rigidities, Fig. 10 shows the flow pattern and deformation of the structure from impact ($t = 0.68$ s) to deposition ($t = 2.5$ s). The deformation of the plastic and steel barriers are shown at the top and bottom, respectively.

At $t = 0.68$ s, only a slight deflection is observed after impact occurs near the crest of the steel barrier (Fig. 10(b)), while obvious deformation at the point of impact is observed for the plastic barrier (Fig. 10(a)). Deformation of the plastic barrier accounts for around 3% of the total barrier height at the peak impact time (Fig. 9). Not only is the deformation enough to attenuate the peak impact pressure, but it also enables the formation of shear bands during the pile-up process. On the contrary, no local barrier deformation is observed for the steel barrier and the granular material is arrested immediately. Therefore, less distinct shear bands are observed in the contours for the steel barrier. Instead, high levels of stress can be seen near the base of the steel barrier at the boundaries. In contrast with the steel barrier, the plastic barrier does not exhibit such contours. At initial impact ($t = 0.68$ s) the maximum deformation is observed near the base of the barrier, but with time, the point of maximum deformation moves upwards along the barrier.

The static pressures behind the rigid and flexible barriers are compared to examine the state of deposited materials. Fig. 11 shows a comparison of the static earth pressures behind the plastic, steel and the rigid reinforced concrete barriers. The stress in the granular assembly is extracted from grids located at the interface between the granular flow and barrier. The height h of each data point along the barrier is normalized by the deposited height at the upstream face of the barrier H_d . Experimental evidence indicates that the mobilization of full passive resistance requires a wall movement in the order of 10–15% of the embedded depth in the case of loose sand; the corresponding mobilization of active pressure is in the order of 1%. Earth pressure comparisons from this study lie between the active and passive states, but much further away from the passive failure line.

For the lateral earth pressure at rest, K_0 is approximated by using the equation proposed by Jaky according to Craig [42] with $\phi = 31^\circ$ [25].

$$K_0 = 1 - \sin\phi' \quad (11)$$

K_0 is calculated to be 0.49, which falls into the typical range of sand between a loose and a dense state (0.35–0.6) as reported by Craig [42].

Both Coulomb and Rankine theory were adopted to calculate the active and passive earth pressures. By using Rankine theory, the active and passive lateral earth pressures are calculated as follows and plotted in Fig. 11:

$$K_a = \frac{1 - \sin\phi'}{1 + \sin\phi'} \quad K_p = \frac{1}{K_a} \quad (12)$$

By using Coulomb theory, the active (K_a) and passive (K_p) earth pressures [43] are calculated as follows:

$$K_a = \frac{\cos^2(\phi' - \alpha)}{\cos^2\alpha \cos(\alpha - \delta) \left\{ 1 - \left[\frac{\sin(\phi' + \delta) \sin(\phi' - \beta)}{\cos(\alpha + \delta) \cos(\alpha - \beta)} \right]^{1/2} \right\}^2}$$

$$K_p = \frac{\cos^2(\phi' + \alpha)}{\cos^2\alpha \cos(\alpha - \delta) \left\{ 1 - \left[\frac{\sin(\phi' + \delta) \sin(\phi' + \beta)}{\cos(\alpha - \delta) \cos(\alpha - \beta)} \right]^{1/2} \right\}^2} \quad (13)$$

where $\alpha = 0$ and the interface friction coefficient between barrier and flow δ is set to be 0.4, the same as flume base. The incline on the retained surface is $\beta = 0$. The active and passive earth pressures are calculated to be 0.33 and 8.7, respectively.

The pressure coefficient of the granular material is expected to be closer to the active pressure coefficient (K_a) due to deformation of the barrier [5]. For the plastic barrier, the maximum deformation is up to 40% of barrier height. The internal strength of the deposited debris

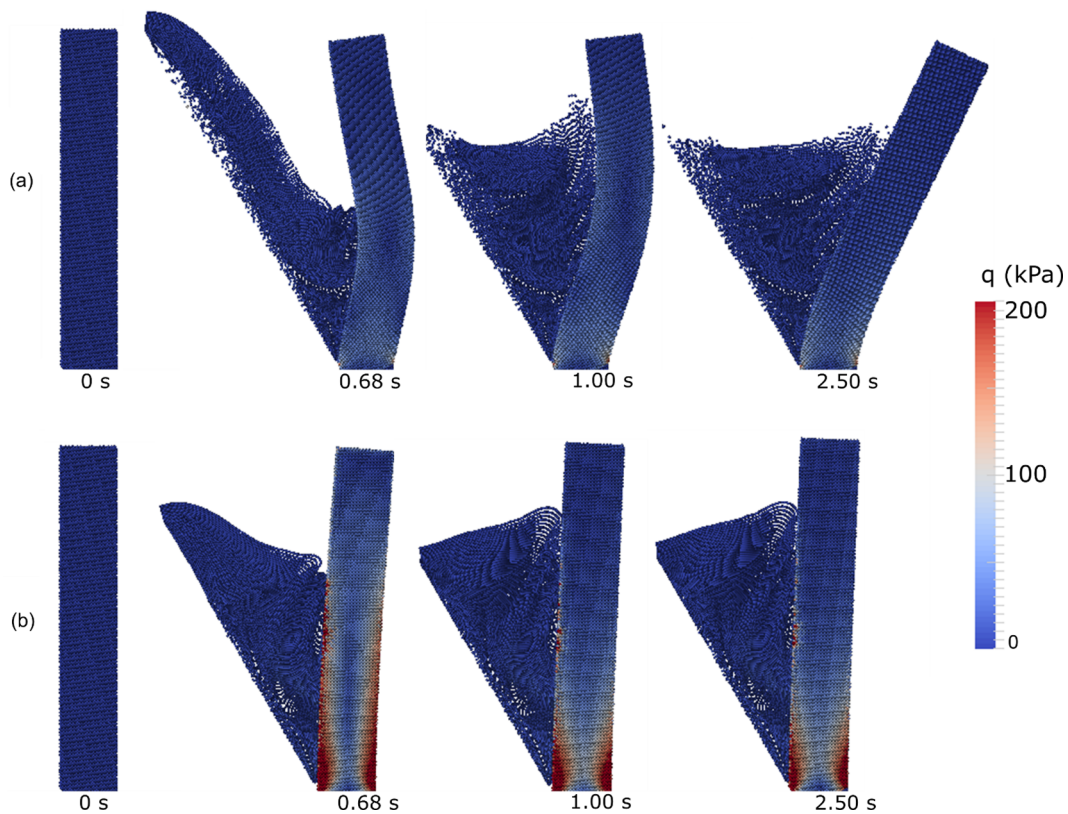


Fig. 10. Computed stress contours: (a) Plastic barrier with $3EI/H^3_{norm} = 2.5 \times 10^{-6}$; (b) Steel barrier with $3EI/H^3_{norm} = 1.0 \times 10^{-4}$.

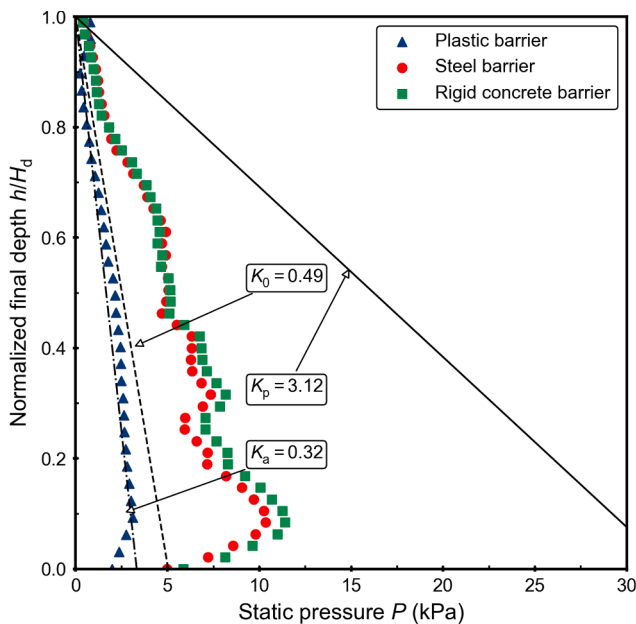


Fig. 11. Computed lateral earth pressure of deposited material.

directly upstream of the plastic barrier is fully mobilized, thereby allowing deposition to reach the state close to an active failure mode. Although the impact process between the granular flow and barrier compresses the flow, deformation of barrier enables an even lower lateral earth pressure acting on a flexible barrier [5,42]. In addition, the effects of arching [43], results in the reduced earth pressure near the bottom of the barrier. The overall distribution of lateral earth pressure of the steel barrier ($3EI/H^3_{norm} = 1.0 \times 10^{-4}$) is greater than that of the K_0 line. This trend is attributed to compression of the granular assembly

during the impact process. The reinforced concrete barrier does not allow any relative movement between the flow and barrier. Thus, larger lateral earth pressures are generated along the barrier. The pressure distribution for all barriers simulated are below the passive earth pressure line, the pressure coefficient is highly influenced by the barrier flexural rigidity. The conservative estimate for static earth pressure can be done by adopting the passive earth pressure coefficient in design process.

4.4. Dissipation of flow energy in granular body

Fig. 12(a) shows the change in energy during the impact process against a reinforced concrete barrier. Each energy type is normalized by the initial potential energy E_0 of the granular material. The datum is at the base of the barrier. The gravitational potential energy decreases as the granular material flows downslope. Part of the potential energy is converted into kinetic energy. Other parts of the potential energy are dissipated by shear between the flow and channel bed and internal shearing of granular assembly. Before impact, both basal and internal shearing do not initially contribute significantly to the overall energy dissipation. The kinetic energy peaks at $t = 0.6$ s and shear between the flowing and deposited material further attenuates the flow kinetic energy. At $t = 1.0$ s, the kinetic energy diminishes, implying that the impact process has reached static equilibrium. At equilibrium conditions, about 50% of the initial energy has dissipated via internal and boundary shearing. The change in energy of a granular flow impacting on the plastic barrier with normalized flexural rigidity $3EI/H^3_{norm} = 2.5 \times 10^{-6}$ is shown in Fig. 12(b). Only 28% of the initial potential energy remains after deposition. Up to 24% of the initial total energy is dissipated due to barrier deformation. Summing the dissipated energy from basal and internal shear, the total energy dissipated within the granular assembly is up to 72% of the initial energy for the case of the plastic barrier. This value is similar to that reported by Ng et al. [5] in their centrifuge model tests of dry sand impacting a flexible

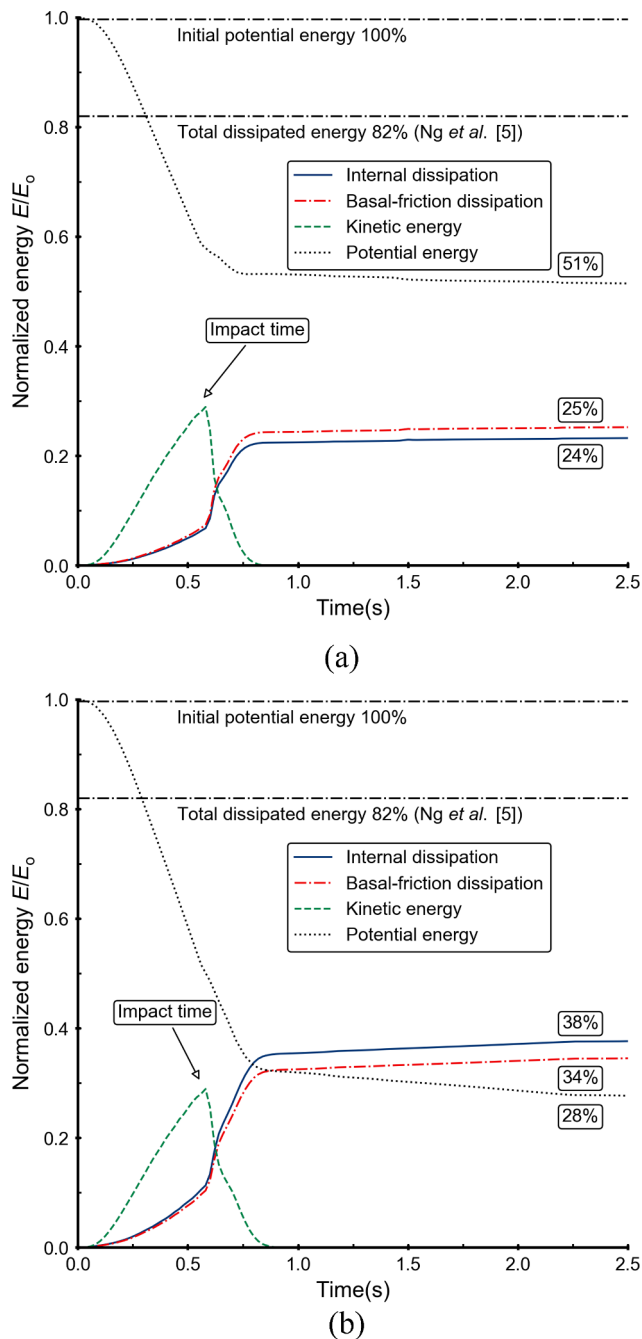


Fig. 12. Computed change in energy for a rigid barrier (a) Reinforced concrete barrier (b) Plastic barrier with normalized flexural rigidity $3EI/H^3_{norm} = 2.5 \times 10^{-6}$.

membrane. In their experiments, they calculated energy dissipation from internal and boundary shear up to 80%.

4.5. Effects of barrier deformation on energy dissipation

Fig. 13(a) shows a comparison of accumulated equivalent shear strain contours of the granular deposition after impact for the plastic and steel barriers respectively. After the granular material had deposited behind the barrier, shear interfaces [44,45] were observed. These shear interfaces coincided with the pile-up process, where layers of sand deposited on material that had already come to rest behind the barrier. Shear interfaces are indicative of dissipation of energy during the layering process. Computed results show obvious shear bands

develop in the granular body. For the plastic barrier ($3EI/H^3_{norm} = 2.5 \times 10^{-6}$), more shear bands are observed. The plastic barrier deflects away from the granular flow, thereby enabling the flow front to climb up on deposited material. As a consequence, subsequent granular flow impacts, overrides and shears the deposited material. Correspondingly, more shearing leads to more energy dissipated within the shear bands. For the steel barrier (Fig. 13(b)), shear bands are evident in the granular assembly. The shear strain mostly occurs near the boundaries of the flume and barrier, while the strain inside deposition is relatively small. The strain contours indicate that granular material is immediately arrested as minimal barrier deformation occurs. Only the upper part of the deposition exhibits some degree of shear. A comparison between the strain contours of a plastic and steel barrier in Fig. 13 shows that the location and length of the shear bands in the deposited material depends on the flexural rigidity of the barrier.

Fig. 14 shows the change in energy during the impact process for different barrier types. An emphasis is placed on the energy dissipated via basal and internal granular shearing. Both kinetic energy and dissipated energy are normalized by the initial potential energy E_0 of the granular mass. Before impact, the kinetic energy is the same for each simulation. After impact, differences in the peak kinetic energy are observed. Higher peak kinetic energies are observed for the stiffer barriers. Meanwhile, the dissipated energy decreases as the barrier stiffness increases. These trends imply that more energy can be dissipated by softer barriers, which enable shear band formation (Fig. 13(a)). With more energy dissipated in the granular assembly, the flow decelerates and cushions the barrier against subsequent impact. More importantly, Fig. 14 shows that for all cases simulated, the dissipated energy increases abruptly at a higher rate when the granular flow impacts the barrier. The abrupt change in energy corresponds to the pile-up process. After initial impact (within 0.2 s from impact), the total dissipated energy plateaus without further barrier deformation. Based on the aforementioned observations, a flexible barrier serves to facilitate shearing during the pile-up process so that more energy can be dissipated to attenuate the peak load.

5. Conclusions

An open-source MPM model implemented with the Drucker-Prager yield criterion associated with a linear elastic model was calibrated using a physical experiment. The calibrated MPM model was then used to study the effects of barrier flexural rigidity on the impact dynamics of granular flows. Findings from this study can be summarized as follows:

- The barrier stiffness highly influence the flow impact loading and energy dissipation process. A threshold $3EI/H^3_{norm} = 6.3 \times 10^{-5}$ (Barrier flexural rigidity is normalized by the stiffness of a typical 1-m thick reinforced concrete cantilever barrier) is identified in this study to demarcate between rigid and deformable barriers. When the barrier stiffness is less than the threshold, the peak flow impact pressure can be effectively attenuated and the loading can be designed according to the static pressure. When the barrier stiffness exceeds the threshold, the barrier behaves like rigid barrier and the design should consider the inertial peak loading through corresponding impact coefficient.
- For softer barriers, relative velocity developed between the barrier and flow. As a result, the flow experiences less compression compared to the steel barrier. Findings imply that by enabling a small displacement of about 3% of barrier height, then the relative velocity and peak impact pressure reduce by up to 40% compared to that of a rigid barrier.
- Relative compression between the flow and barrier governs velocity of wave propagation inside the granular material. Softer barriers give less compression to the flow body, leading to smaller propagation velocities compared to that of a steel barrier.
- Around 85% of the dissipated energy occurs during the pile-up

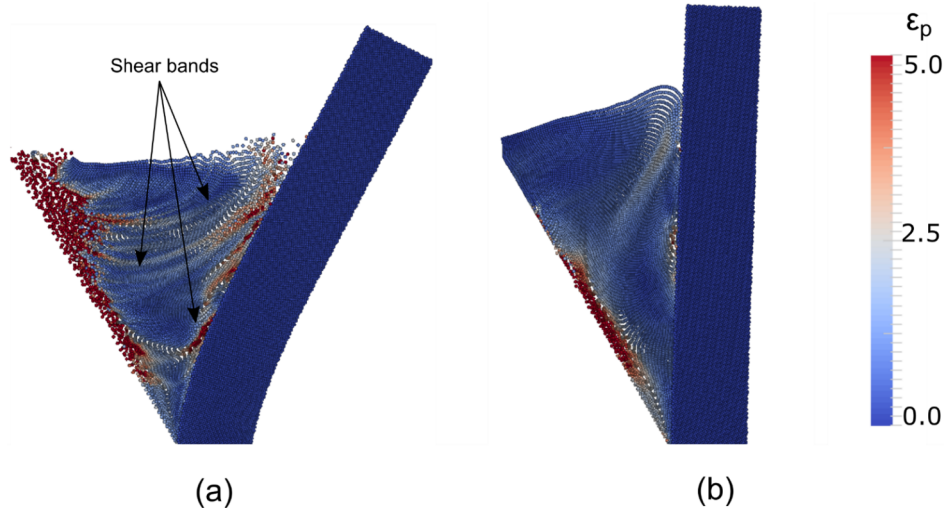


Fig. 13. Equivalent shear strain ϵ_p inside the granular body, (a) Plastic barrier with $3EI/H^3_{norm} = 2.5 \times 10^{-6}$ and (b) Steel barrier with $3EI/H^3_{norm} = 1.0 \times 10^{-4}$.

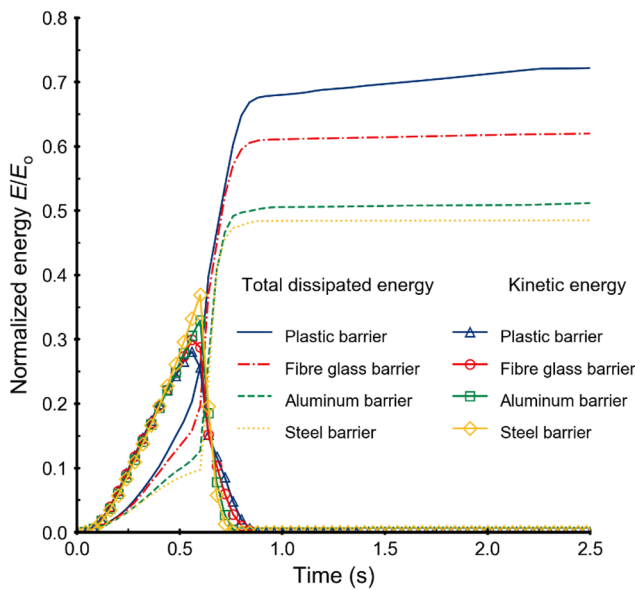


Fig. 14. Energy dissipated inside the granular body for different barriers.

process, the interaction between the incoming flow and deposited material along the slip interface is effective in dissipating flow kinetic energy. A flexible barrier facilitates longer shearing interface during the pile-up process, thereby dissipating more energy compared to that of rigid barriers. Furthermore, barrier designs should utilize the internal dissipation inside flow by providing a finite amount of deformation during impact.

Appendix A. Velocity update scheme

At the end of each time step, the velocity on each node is projected back to the material points. Two conventional velocity update schemes are combined, specifically the Particle In Cell (PIC) and Fluid Implicit Particle (FLIP), which are given as follows:

$$\text{PIC update: } \mathbf{v}_{p,\text{PIC}}^{n+1} = \sum_I \mathbf{v}_I^{n+1} S_{Ip}$$

$$\text{FLIP update: } \mathbf{v}_{p,\text{FLIP}}^{n+1} = \mathbf{v}_p^n + \Delta t \sum_I \mathbf{a}_I^{n+1} S_{Ip}$$

CRediT authorship contribution statement

C.W.W. Ng: Funding acquisition, Project administration, Supervision, Writing - review & editing, Conceptualization, Investigation. **C. Wang:** Software, Data curation, Visualization, Writing - original draft, Formal analysis. **C.E. Choi:** Project administration, Supervision, Writing - original draft, Writing - review & editing, Conceptualization, Investigation. **W.A.R.K. De Silva:** Writing - review & editing. **S. Poudyal:** Writing - review & editing.

Declaration of Competing Interest

The authors declare that they have no known competing financial interests or personal relationships that could have appeared to influence the work reported in this paper.

Acknowledgements

The work described in this paper was partially supported by a grant from the Research Grants Council of the Hong Kong Special Administrative Region, China (Project Nos. AoE/E-603/18; T22-603/15N; 16209717; 16212618). The authors would like to thank the support from the National Natural Science Foundation of China (51709052). Finally, the authors are grateful for the support of the HKUST Jockey Club Institute for Advanced Study. The authors would like to thank the financial support by the Hong Kong Jockey Club Disaster Preparedness and Response Institute (HKJCDPRI18EG01). S. Poudyal gratefully acknowledges the support of Hong Kong PhD Fellowship Scheme (HKPFS) provided by the RGC of HKSAR.

where $\mathbf{v}_{p,PIC}^{n+1}$ and $\mathbf{v}_{p,FLIP}^{n+1}$ are the updated velocities based on PIC and FLIP, respectively. \mathbf{v}_p^n represents the material point velocity at the previous time step and \mathbf{a}_I^{n+1} is the acceleration at nodal point I. PIC directly uses the nodal velocity to update the material point velocity, which can enhance global simulation stability but suffer from over dissipation of energy. In contrast, FLIP updates the material point velocity by using the acceleration from nodal points, which can avoid excessive energy dissipation but result in noise due to the mapping procedure.

A suitable combination of PIC and FLIP has been adopted to significantly improve the performance of the MPM simulations [21]:

$$\mathbf{v}_p^{n+1} = \alpha_{PIC} \mathbf{v}_{p,PIC}^{n+1} + (1 - \alpha_{PIC}) \mathbf{v}_{p,FLIP}^{n+1}$$

where \mathbf{v}_p^{n+1} denotes the updated particle velocity based on a linear combination of PIC and FLIP, α_{PIC} is the PIC fraction in the particle velocity update: $\alpha_{PIC} = 1$ represents only PIC velocity update, whilst $\alpha_{PIC} = 0$ implies only FLIP velocity update.

Appendix B. Contact algorithm and frictional slip surface

MPM can naturally handle non-slip contact between different bodies [30]. The reason for this is that a single-valued velocity field automatically prevents particle-particle penetration. This non-slip feature can only model contact by stick conditions meaning surfaces move in the same velocity field when in contact but move independently when apart. However, many contact problems frictional sliding occurs at the contact surface. Thus, a contact algorithm is required. Bardenhagen et al. [29] proposed an algorithm which relaxes the no-slip condition and allows Coulomb friction and slip at contacting boundary nodes. This frictional contact algorithm was further developed by Nairn [20] has been applied in soil-structure simulations and illustrated as follows:

- Detect the contact:

Improved contact calculations are looking at material positions and calculating separation of material surfaces using

$$\delta_n = (\mathbf{x}_{i,a} - \mathbf{x}_{i,b}) \cdot \mathbf{n} - 0.8h_\perp$$

Where \mathbf{n} is the surface normal, the subtraction of $0.8h_\perp$ accounts for the spatial effect that particle surfaces come into contact before the centers. For a regular grid with equal element dimension in all directions, h_\perp is equal to element size Δx .

If the material starts out in contact,

A useful method is to change the separation calculation by using particle displacements. In this approach, the position extrapolation is changed to a displacement extrapolation:

$$m_{ij} \Delta x_{i,j} = \sum_{p \in j} S_{ip} m_p (\mathbf{x}_p - \mathbf{x}_p^{(0)})$$

the surface separation is found from extrapolated displacements of objects a and b as follows:

$$\delta_n = (\Delta x_{i,a} - \Delta x_{i,b}) \cdot \mathbf{n}$$

- Find the contact area

the contact area at node i for 2D case in terms of extrapolated quantities defined above is :

$$A_{cell} = \frac{t \sqrt{2\Omega_i \min(\Omega_{i,a}, \Omega_{i,b})}}{h_\perp}$$

(nodal domains at node i and j would be $\Omega_{i,a} = \Omega_{i,b} = A_{cell}/2$, $A_{cell} = \Delta x \Delta y$)

- Implementing contact mechanics

When contact surfaces are determined to be in contact, the final task is to modify nodal momenta and forces to reflect to implemented contact mechanics.

Calculate the momentum change applied to material a that would be required for that material to move in the center of mass velocity $\mathbf{v}_i^{(c)}$

Where

$$\mathbf{v}_i^{(c)} = \frac{\sum_j \mathbf{P}_{i,j}}{m_i^{(c)}} = \frac{m_{i,a} \mathbf{v}_{i,a} + m_{i,b} \mathbf{v}_{i,b}}{m_{i,a} + m_{i,b}}$$

$$\Delta \mathbf{P}_{i,a} = m_{i,a} \mathbf{v}_i^{(c)} - \mathbf{P}_{i,a} = \frac{m_{i,a} \mathbf{P}_{i,b} - m_{i,b} \mathbf{P}_{i,a}}{m_{i,a} + m_{i,b}}$$

if $\Delta \mathbf{P}_{i,a}$ was applied to material a and $-\Delta \mathbf{P}_{i,a}$ applied to material b, the two materials would stick together.

The difference in unmodified velocities for materials a and b can be related to this momentum change:

$$\Delta \mathbf{v}_i = \mathbf{v}_{i,b} - \mathbf{v}_{i,a} = \frac{\mathbf{P}_{i,b}}{m_{i,b}} - \frac{\mathbf{P}_{i,a}}{m_{i,a}} = \frac{\Delta \mathbf{P}_{i,a}}{m_{i,red}}$$

$$m_{i,red} = \frac{m_{i,a} m_{i,b}}{m_{i,a} + m_{i,b}}$$

the momentum change can be interpreted as apparent contacting forces by rewriting $\Delta P_{i,a}$ as

$$\Delta P_{i,a} = (\Delta P_{i,a} \cdot \mathbf{n}) \mathbf{n} + (\Delta P_{i,a} \cdot \mathbf{t}) \mathbf{t} = (-N A_c \Delta t) \mathbf{n} + (S_{stick} A_{cell} \Delta t) \mathbf{t}$$

Where A_{cell} is contact area calculated above, and the $N = -\frac{\Delta P_{i,a} \cdot \mathbf{n}}{A_{cell} \Delta t}$ and $S_{stick} = \frac{\Delta P_{i,a} \cdot \mathbf{t}}{A_{cell} \Delta t}$.

To implement friction, we calculate the tangential traction as the function of normal pressure:

1. If $S_{stick} < S_{slide}$, then the driving forces for frictional sliding are too small to overcome sticking. Set final momentum change to $\Delta P'_{i,a} = \Delta P_{i,a}$
2. If $S_{stick} > S_{slide}$, the surface would slide.

Set the final momentum change to $\Delta P'_{i,a} = (-N A_{cell} \Delta t) \mathbf{n} + (S_{slide} A_{cell} \Delta t) \mathbf{t}$

3. Change the momenta for materials a and b to

$$\mathbf{P}'_{i,a} = \mathbf{P}_{i,a} + \Delta \mathbf{P}'_{i,a} \text{ and } \mathbf{P}'_{i,b} = \mathbf{P}_{i,b} - \Delta \mathbf{P}'_{i,a}$$

4. To keep forces consistent with changed momenta in contact calculations done after updating nodal momenta, the nodal forces should be changed to:

$$\mathbf{f}'_{i,a} = \mathbf{f}_{i,a} + \frac{\Delta \mathbf{P}'_{i,a}}{\Delta t} \text{ and } \mathbf{f}'_{i,b} = \mathbf{f}_{i,b} - \frac{\Delta \mathbf{P}'_{i,a}}{\Delta t}$$

Appendix C. Convergency of the impact force

The contact force is calculated based on the momentum exchange at the grid nodes (Appendix B), which are all located along the interface between two materials in contact. We identified the material points along the interface and then extracted the stress from those material points. The effects of selecting a different number of layers of material points can be shown in Fig. 15. As we can see from the Fig. 15, the impact force gradually increases as the granular flow approaches the barrier. All three selections are able to reflect the general trend. A single layer of material points gives the largest magnitude among the three selections. Selection of two and three layers of material points shows around 9% and 15% decrease, respectively, in extracted impact force. The decrease in force is expected as the selection of three layers of points would involve more points further away from the barrier compared to the single layer. If more layers are used, then the impact stress would deviate too much from the actual value near the impact region. On the other hand, a single layer exhibits more oscillation of extracted pressure compared to two and three layers. This is attributed to the intensive momentum exchange between two objects and limited material points used in the simulation. More layers mean that more material points are involved for averaging the force and can suppress the numerical oscillation in the impact area. In order to give a meaningful profile of the impact force, two layers of material points are selected to avoid magnitude decrease and numerical oscillation.

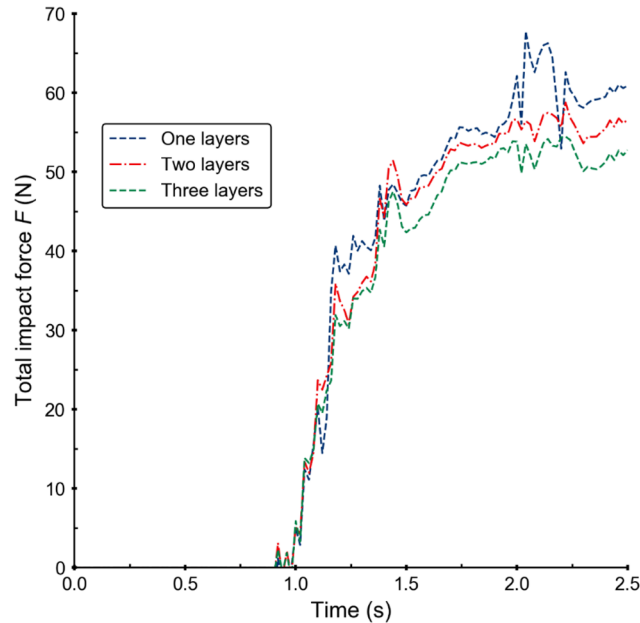


Fig. 15. Time history of impact pressure extracted from different layers of material points.

References

- [1] Chen X, Cui P, You Y, Chen J, Li D. Engineering measures for debris flow hazard mitigation in the Wenchuan earthquake area. *Eng Geol* 2015;194:73–85. <https://doi.org/10.1016/j.enggeo.2014.10.002>.
- [2] Hürlimann M, Copons R. Detailed debris flow hazard assessment in Andorra: a multidisciplinary approach. *Geomorphology* 2006;78:359–72.
- [3] Wendeler C, Volkwein A, Roth A, Denk M, Wartmann S. Field measurements used for numerical modelling of flexible debris flow barriers. In: Chen CL, Major J, editors. *Debris-Flow Hazards Mitig. Mech. Predict.* 2007. p. 681–7.
- [4] Kwan JSH, Cheung RWM. Discussion note suggestions on design approaches for flexible debris-resisting barriers; 2012.
- [5] Ng CWW, Song DECC, Kwan JSH, Shiu HYK, Koo RCH. Centrifuge modelling of dry granular and viscous impact on rigid and flexible barriers. *Can Geotech J* 2016;19:1–19.
- [6] Moriguchi S, Borja RI, Yashima A, Sawada K. Estimating the impact force generated by granular flow on a rigid obstruction. *Acta Geotech* 2009;4:57–71. <https://doi.org/10.1007/s11440-009-0084-5>.
- [7] Jiang YJ, Fan XY, Li TH, Xiao SY. Influence of particle-size segregation on the impact of dry granular flow. *Powder Technol* 2018;340:39–51. <https://doi.org/10.1016/j.powtec.2018.09.014>.
- [8] Albaba A, Lambert S, Faug T. Dry granular avalanche impact force on a rigid wall: Analytic shock solution versus discrete element simulations. *Phys Rev E* 2018;97:1–12. <https://doi.org/10.1103/PhysRevE.97.052903>.
- [9] Song D, Zhou GGD, Xu M, Choi CE, Li S, Zheng Y. Quantitative analysis of debris-flow flexible barrier capacity from momentum and energy perspectives. *Eng Geol* 2019;251:81–92. <https://doi.org/10.1016/j.enggeo.2019.02.010>.
- [10] Zhan L, Peng C, Zhang B, Wu W. Three-dimensional modeling of granular flow impact on rigid and deformable structures. *Comput Geotech* 2019;112:257–71. <https://doi.org/10.1016/j.compgeo.2019.03.019>.
- [11] Savage SB, Hutter K. The motion of a finite mass of granular material down a rough incline. *J Fluid Mech* 1989;199:177–215. <https://doi.org/10.1017/S0022112089000340>.
- [12] Hungr O. A model for the runout analysis of rapid flow slides, debris flows, and avalanches. *Can Geotech J* 1995;32:610–23.
- [13] George DL, Iverson RM. A depth-averaged debris-flow model that includes the effects of evolving dilatancy. II. Numerical predictions and experimental tests A depth-averaged debris-flow model that includes the effects of evolving dilatancy. II. Numerical predictions and exper. *Proc R Soc A Math Phys Eng Sci* 2014;470:1–31. <https://doi.org/10.1098/rspa.2013.0820>.
- [14] Li X, Zhao J. A unified CFD-DEM approach for modeling of debris flow impacts on flexible barriers. *Int J Numer Anal Methods Geomech* 2018;42:1643–70. <https://doi.org/10.1002/nag.2806>.
- [15] Iverson RM. Scaling and design of landslide and debris-flow experiments. *Geomorphology* 2015;244:9–20. <https://doi.org/10.1016/j.geomorph.2015.02.033>.
- [16] Ceccato F, Redaelli I, di Prisco C, Simonini P. Impact forces of granular flows on rigid structures: Comparison between discontinuous (DEM) and continuous (MPM) numerical approaches. *Comput Geotech* 2018;103:201–17. <https://doi.org/10.1016/j.compgeo.2018.07.014>.
- [17] Mast CM, Arduino P, Miller GR, Mackenzie-Helnwein P. Avalanche and landslide simulation using the material point method: flow dynamics and force interaction with structures. *Comput Geosci* 2014;18:817–30. <https://doi.org/10.1007/s10596-014-9428-9>.
- [18] Dunatunga S, Kamrin K. Continuum modelling and simulation of granular flows through their many phases. *J Fluid Mech* 2015;779:483–513. <https://doi.org/10.1017/jfm.2015.383>.
- [19] Ceccato F, Beuth L, Simonini P. Analysis of piezocone penetration under different drainage conditions with the two-phase material point method. *J Geotech Geoenviron Eng* 2016;142:04016066. [https://doi.org/10.1061/\(ASCE\)GT.1943-5606.0001550](https://doi.org/10.1061/(ASCE)GT.1943-5606.0001550).
- [20] Nairn JA. Modeling imperfect interfaces in the material point method using multimaterial methods. *Comput Model Eng Sci* 2013;92:271–99.
- [21] Nairn JA. Numerical simulation of orthogonal cutting using the material point method. *Eng Fracture Mech* 2015;149:262–75.
- [22] Guo YJ, Nairn JA. Simulation of dynamic 3D crack propagation within the material point method. *Comput Model Eng Sci* 2017;113:389–410.
- [23] Lorenzo R, Cunha RP, Cordao-Neto MP, Nairn J. Numerical simulation of the installation of jacked piles in sand with the material point method. *Can Geotech J* 2018;55(1):131–46. <https://doi.org/10.1139/cgj-2016-0455>.
- [24] Liang W, Zhao J. Multiscale modeling of large deformation in geomechanics. *Int J Numer Anal Methods Geomech* 2019;43:1080–114. <https://doi.org/10.1002/nag.2921>.
- [25] Ng CWW, Choi CE, Liu LHD, Wang Y, Song D, Yang N. Influence of particle size on the mechanism of dry granular run-up on a rigid barrier. *Géotechnique Lett* 2017;7:79–89. <https://doi.org/10.1680/jgele.16.00159>.
- [26] Sulsky D, Chen Z, Schreyer HL. A particle method for hystory-dependent materials. *Comput Methods Appl Mech Eng* 1994;118:179–96. [https://doi.org/10.1016/0045-7825\(94\)90112-0](https://doi.org/10.1016/0045-7825(94)90112-0).
- [27] Sołowski WT, Sloan SW. Evaluation of material point method for use in geotechnics. *Int J Numer Anal Methods Geomech* 2015;39:685–701. <https://doi.org/10.1002/nag.2321>.
- [28] Zhang X, Chen Z, Liu Y. The material point method: a continuum-based particle method for extreme loading cases; 2016.
- [29] Bardenhagen S, Brackbill J, Sulsky D. The material-point method for granular materials. *Comput Methods in Appl Mech and Eng* 2000;187:529–41.
- [30] Nairn JA, Bardenhagen SG, Smith GD. Generalized contact and improved frictional heating in the material point method. *Comput Part Mech* 2017:1–12.
- [31] Bui HH, Fukagawa R, Sako K, Ohno S. Lagrangian meshfree particles method (SPH) for large deformation and failure flows of geomaterial using elastic-plastic soil constitutive model. *Int J Numer Anal Methods Geomech* 2008;32:1537–70. <https://doi.org/10.1002/nag.688>.
- [32] Soga K, Alonso E, Yerro A, Kumar K, Bandara S. Trends in large-deformation analysis of landslide mass movements with particular emphasis on the material point method. *Géotechnique* 2016;66:248–73. <https://doi.org/10.1680/jgeot.15.LM.005>.
- [33] White D, Take W, Bolton MD. Soil deformation measurement using particle image velocimetry (PIV) and photogrammetry. *Géotechnique* 2003;53(7):619–31.
- [34] Chanut B, Faug T, Naaim M. Time-varying force from dense granular avalanches on a wall. *Phys Rev E* 2010;82: 041302.
- [35] Thielicke W, Stamhuis E. PIVlab—towards user-friendly, affordable and accurate digital particle image velocimetry in MATLAB. *J Open Research Software* 2014.
- [36] Brighenti R, Segalini A, Ferrero AM. Debris flow hazard mitigation: A simplified analytical model for the design of flexible barriers. *Comput Geotech* 2013;54:1–15. <https://doi.org/10.1016/j.compgeo.2013.05.010>.
- [37] Sze EH, Koo RC, Leung JM, Ho KK. Design of flexible barriers against sizeable landslides in Hong Kong. *HKIE Trans* 2018;25:115–28.
- [38] Jóhannesson T, Gauer P, Issler P, Lied K. The design of avalanche protection dams: recent practical and theoretical developments; 2009.
- [39] Bandara S, Soga K. Coupling of soil deformation and pore fluid flow using material point method. *Comput Geotech* 2015;63:199–214. <https://doi.org/10.1016/j.compgeo.2014.09.009>.
- [40] Lv Y, Ng CWW, Wang Y. Evaluation of wave dissipation in sand under impact loading. *J Geotech Geoenviron Eng* 2019;145:06019007. [https://doi.org/10.1061/\(ASCE\)GT.1943-5606.0002104](https://doi.org/10.1061/(ASCE)GT.1943-5606.0002104).
- [42] Craig R. *Craig's soil mechanics*; 2004.
- [43] Ashwood W, Hungr O. Estimating total resisting force in flexible barrier impacted by a granular avalanche using physical and numerical modeling. *Can Geotech J* 2016;53:1700–17. <https://doi.org/10.1139/cgj-2015-0481>.
- [44] Schall P, van Hecke M. Shear bands in matter with granularity. *Annual Rev Fluid Mech* 2010;42:67–88. <https://doi.org/10.1146/annurev-fluid-121108-145544>.
- [45] Fenistein D, van de Meent JW, van Hecke M. Universal and wide shear zones in granular bulk flow. 094301 *Phys RevLett* 2004;92. <https://doi.org/10.1103/PhysRevLett.92.094301>.